

# THE REST FRAME ULTRAVIOLET SPECTRA OF UV-SELECTED ACTIVE GALACTIC NUCLEI AT $Z \sim 2 - 3$ <sup>1</sup>

KEVIN N. HAINLINE, ALICE E. SHAPLEY<sup>2</sup>

Department of Astronomy, University of California, Los Angeles, 430 Portola Plaza, Los Angeles, CA 90024

JENNY E. GREENE

Department of Astronomy, University of Texas, Austin, TX 78712

CHARLES C. STEIDEL

California Institute of Technology, MS 105-24, Pasadena, CA 91125

*Received DATE; accepted DATE*

## ABSTRACT

We present new results for a sample of 33 narrow-lined UV-selected active galactic nuclei (AGNs), identified in the course of a spectroscopic survey for star-forming galaxies at  $z \sim 2 - 3$ . The rest-frame UV composite spectrum for our AGN sample shows several emission lines characteristic of AGNs, as well as interstellar absorption features detected in star-forming LBGs. We report a detection of N IV]  $\lambda 1486$ , which has been observed in high-redshift radio galaxies, as well as in rare optically-selected quasars. The UV continuum slope of the composite spectrum is significantly redder than that of a sample of non-AGN UV-selected star forming galaxies. Blueshifted Si IV absorption provides evidence for outflowing highly-ionized gas in these objects at speeds of  $\sim 10^3$  km s<sup>-1</sup>, quantitatively different from what is seen in the outflows of non-AGN LBGs. Grouping the individual AGN by parameters such as Ly $\alpha$  equivalent width, redshift, and UV continuum magnitude allows for an analysis of the major spectroscopic trends within the sample. Stronger Ly $\alpha$  emission is coupled with weaker low-ionization absorption, which is similar to what is seen in the non-AGN LBGs, and highlights the role that cool interstellar gas plays in the escape of Ly $\alpha$  photons. However, the AGN composite does not show the same trends between Ly $\alpha$  strength and extinction seen in the non-AGN LBGs. These results represent the first such comparison at high-redshift between star-forming galaxies and similar galaxies that host AGN activity.

*Subject headings:* cosmology: observations – galaxies: evolution – galaxies: high-redshift – galaxies: active galactic nuclei

## 1. INTRODUCTION

In order to explain observations of massive galaxy evolution in the universe, current models of galaxy formation require a form of energetic feedback that is thought to result from the effects of a central active galactic nucleus (AGN) (Croton et al. 2006; Somerville et al. 2008; Di Matteo et al. 2008). Energy and momentum input from the AGN into the galaxy’s interstellar medium (ISM) can serve to heat or remove gas so that it is no longer available for star formation. “AGN feedback” has been presented as one of the major factors giving rise to the red sequence in massive galaxies (Silk & Rees 1998; Kauffmann et al. 2003). Furthermore, every galaxy bulge appears to contain a supermassive black hole (Kormendy & Richstone 1995), whose mass is correlated with bulge properties such as stellar velocity dispersion (Merritt & Ferrarese 2001; Gültekin et al. 2009). These correlations offer evidence of coupling between the for-

mation of the black hole and bulge, which may result from the effects of AGN feedback (Silk & Rees 1998; Murray et al. 2005; Hopkins et al. 2008). Outflows have been observed in strongly star-forming galaxies over a range of redshifts (Franx et al. 1997; Shapley et al. 2003; Martin 2005; Steidel et al. 2010; Rupke et al. 2005a), and post-starburst galaxies at  $z \sim 0.6$  (Tremonti et al. 2007). For AGNs, outflows have been observed in local Seyfert galaxies (Crenshaw et al. 2003; Krug et al. 2010), and at higher redshifts in broad absorption line quasars (Korista et al. 2008; Ganguly & Brotherton 2008), radio galaxies (Nesvadba et al. 2006, 2008), and ULIRGs (Alexander et al. 2010). However, at early times, outflows have thus far not been fully examined in a sample of active galaxies that can be quantitatively compared to a non-active sample with similar host galaxy properties. This paper examines the outflow properties of such a sample at  $2 \leq z \leq 3$ , when both star-formation density and black hole (BH) accretion were at their peak (Madau et al. 1996; Ueda et al. 2003; Richards et al. 2006; Reddy et al. 2008; Silverman et al. 2008).

The rest-frame UV portion of a galaxy spectrum is ideally suited for the study of the ISM. In star-forming

<sup>1</sup> Based, in part, on data obtained at the W.M. Keck Observatory, which is operated as a scientific partnership among the California Institute of Technology, the University of California, and NASA, and was made possible by the generous financial support of the W.M. Keck Foundation.

<sup>2</sup> David and Lucile Packard Fellow

galaxies, this spectral region contains emission or absorption from H I Lyman  $\alpha$ , as well as low- and high-ionization metal absorption lines that have been used to infer the presence of outflows (Pettini et al. 2000, 2001, 2002; Shapley et al. 2003). At  $z \sim 2 - 3$ , the rest-frame UV part of the spectrum is shifted into the observed optical, and is accessible using ground-based facilities. At these redshifts, individual galaxy spectra have low continuum signal-to-noise (S/N), which makes robust absorption line measurements challenging. With a large enough sample, however, a higher S/N composite spectrum can be created, allowing measurements of the global properties and spectral trends within the sample. Shapley et al. (2003) and Steidel et al. (2010) have used such composite spectra to explore the outflow properties of UV-selected star-forming galaxies at  $z \sim 2 - 3$ .

Because the black hole accretion disk and broad-line region are obscured from view, the light from a narrow-lined AGN is not dominated by emission from the central source, but rather that of the host galaxy. The ability to study the host galaxy allows for a comparison between the galaxy-scale properties of a sample of narrow-lined AGNs and those of a similar non-AGN sample. In order to undertake such a study, we augment the sample of narrow-lined UV-selected AGNs at  $z \sim 3$  presented in Steidel et al. (2002), extending it to include objects at  $z \sim 2$ . The original sample enabled, for the first time, an estimation of the fraction of star forming galaxies within the Lyman Break Galaxy (LBG) survey that showed evidence for AGN activity on the basis of their rest frame UV spectroscopic properties. With the expanded sample of AGNs, we construct composite spectra that reveal the properties of outflowing gas in these objects. The galaxies that harbor these narrow-lined AGN were selected on the basis of their broadband rest-frame UV colors, and should have host galaxies similar to those of the non-AGN LBGs. As this AGN sample appears to be hosted by galaxies drawn from the same parent population as the non-AGN LBG sample (Steidel et al. 2002; Adelberger & Steidel 2005), we can conduct a controlled experiment to understand how the AGN impacts the gas properties of the host galaxy.

The sample of UV-selected AGNs is presented in §2, while in §3 we describe the creation of the AGN composite spectrum. This spectrum and its basic properties are shown in §4, including the detection of blueshifted high-ionization absorption features. In §5, we examine spectral trends within the AGN sample that are highlighted by separating objects according to Ly $\alpha$  equivalent width (EW), UV magnitude, and redshift. We conclude in §6 with a discussion placing the results from the composite spectrum analysis into the context of our understanding of AGNs. Throughout our analysis, we assume  $\Omega_M = 0.27$ ,  $\Omega_\Lambda = 0.73$ , and  $H_0 = 71 \text{ km s}^{-1} \text{ Mpc}^{-1}$ .

## 2. THE UV-SELECTED AGN SAMPLE AND OBSERVATIONS

The narrow-lined AGNs used to construct the composite spectra were discovered in the course of a survey of  $z \sim 2 - 3$  UV-selected galaxies. This survey spans 0.89 degrees<sup>2</sup> across 29 fields and is described in detail in Steidel et al. (2003, 2004) and Reddy et al. (2008). The method for selecting  $z \sim 3$  LBGs is based on the fact that the intervening intergalactic medium absorbs most

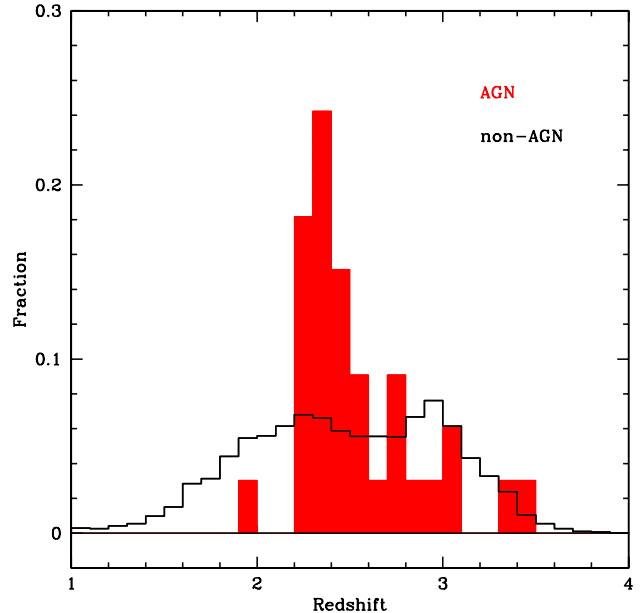


FIG. 1.— The normalized redshift distribution for our sample of UV-selected narrow-lined AGNs, compared to the redshifts of the  $z \sim 2 - 3$  UV-selected non-AGN sample.

of the photons with wavelengths shortward of the Lyman break at 912 Å. At  $z \sim 3$ , the Lyman break is shifted to optical wavelengths, and galaxies at this redshift are selected by their position in a  $U - G$  vs.  $G - R$  color-color diagram. As described in Steidel et al. (2004) and Adelberger et al. (2004), color criteria have also been developed to identify galaxies with similar intrinsic rest-frame UV colors to the  $z \sim 3$  LBGs, but at  $z \sim 2$ . At this redshift, the observed  $UGR$  colors reflect a flat part of the spectrum redward of the Lyman break for star-forming galaxies. The survey of  $z \sim 2 - 3$  UV-selected galaxies is split into various subsamples based on redshift, including the “BM” ( $1.5 \leq z \leq 2.0$ ), “BX” ( $2.0 \leq z \leq 2.5$ ), and the “C”, “D”, and “MD” galaxies ( $2.7 \leq z \leq 3.3$ ). From the photometric sample, objects were selected for spectroscopy without regard for their x-ray or morphological properties. Therefore, the fraction of candidates targeted for spectroscopy should be similar for both AGNs and star-forming galaxies in the UV-selected photometric sample.

The parent UV-selected spectroscopic sample consists of 3059 galaxies, 48 broad-lined AGN, and 33 narrow-lined AGN (which comprise 1% of the sample). Objects were identified as narrow-lined AGN if they showed strong Ly $\alpha$  emission accompanied by significant emission in either N V  $\lambda 1240$  or C IV  $\lambda 1549$ , where the FWHM for any of the emission features was less than 2000 km s<sup>-1</sup>. In some objects, Si IV  $\lambda\lambda 1393, 1402$  or He II  $\lambda 1640$  was additionally used to indicate the presence of an AGN. In practice, the requirement of strong Ly $\alpha$  emission does not select against finding AGNs with strong nebular emission lines but weak Ly $\alpha$  emission. In the sample of AGNs presented here, Ly $\alpha$  is on average  $\sim 4 - 5$  times stronger than C IV, which is typically the next strongest feature. Furthermore, no objects were found in the parent sample of UV-selected galaxies with high-ionization emission lines while lacking Ly $\alpha$  emission. The AGN sample pre-

TABLE 1  
UV-SELECTED NARROW-LINED AGN SAMPLE

FIELD	OBJECT	RA (J2000)	DEC (J2000)	$\mathcal{R}$ (mag)	$z_{Ly\alpha}$ <sup>a</sup>	Emission Line Detections			
Q0000	C7	00:03:28.85	-26:03:53.3	24.21	3.431	NV	CIV	HeII	CIII]
Q0000	C14	00:03:30.39	-26:01:20.7	24.47	3.057	NV	CIV	HeII	n.c. <sup>b</sup>
CDFb	D3	00:53:43.02	12:22:02.5	24.75	2.777	NV	CIV	HeII	CIII]
Q0100	BX172	01:03:08.46	13:16:41.7	23.50	2.312	NV	CIV	HeII	n.c.
Q0142	BX186	01:45:17.47	-09:45:08.0	25.18	2.361	...	CIV	...	n.c.
Q0142	BX195	01:45:17.68	-09:44:54.2	23.56	2.382	NV	CIV	HeII	n.c.
Q0142	BX256	01:45:15.74	-09:42:12.5	23.91	2.321	NV	n.c.	n.c.	n.c.
Q0201	oC12	02:03:56.16	11:36:30.1	24.83	2.357	NV	CIV	HeII	...
Q0256	md37	02:59:02.21	00:12:03.4	24.06	2.803	NV	CIV	...	CIII]
Q0933	MD38	09:33:48.60	28:44:32.3	22.61	2.763	...	CIV	HeII	n.c.
Q1217	BX46	12:19:19.94	49:40:22.7	23.85	1.980	NV	...	...	n.c.
HDF	MMD12	12:37:19.80	62:09:56.0	24.36	2.648	NV	CIV	...	CIII]
HDF	BMZ1156	12:37:04.34	62:14:46.3	24.62	2.211	NV	CIV	HeII	CIII]
HDF	BMZ1384	12:37:23.15	62:15:38.0	23.98	2.243	NV	CIV	HeII	CIII]
HDF	BX160	12:37:20.07	62:12:22.7	24.02	2.461	NV	CIV	...	...
Westphal	MM47	14:17:57.39	52:31:04.5	24.30	3.027	...	CIV	HeII	n.c.
Westphal	MMD58	14:17:18.29	52:28:53.9	25.36	2.596	...	n.c. <sup>d</sup>	HeII	...
Q1422	d14	14:24:47.44	22:48:04.3	24.30	2.245	NV	CIV	...	CIII]
Q1422	c73	14:24:46.41	22:55:45.5	24.88	3.382	NV	n.c.	n.c.	n.c.
Q1422	md109	14:24:42.58	22:54:46.6	23.69	2.229	NV	CIV	HeII	CIII]
Q1623	BX151	16:25:29.61	26:53:45.0	24.60	2.441	NV	CIV	HeII	n.c.
Q1623	BX454	16:25:51.42	26:43:46.3	23.89	2.422	NV	CIV	...	...
Q1623	BX663	16:26:04.58	26:48:00.2	24.14	2.435	NV	CIV	HeII	...
Q1623	BX747	16:26:13.46	26:45:53.2	22.55	2.441	NV	CIV	HeII	n.c.
Q1623	BX827	16:26:19.31	26:45:15.3	25.15	2.506	...	CIV	...	n.c.
Q1700	MD157	17:00:52.19	64:15:29.3	24.35	2.295	NV	CIV	HeII	CIII]
Q1700	MD174	17:00:54.54	64:16:24.8	24.56	2.347	NV	...	...	n.c.
Q2233	D3	22:36:16.12	13:55:19.2	23.93	2.795	NV	CIV	HeII	CIII]
Q2233	MD21	22:36:35.83	13:55:42.0	24.80	2.549	NV	CIV	HeII	n.c.
DSF2237a	D11	22:40:02.99	11:52:13.9	25.19	2.959	...	CIV	HeII	CIII]
DSF2237b	MD53	22:39:28.67	11:52:09.5	24.07	2.292	...	CIV	HeII	CIII]
Q2343	BX333	23:46:21.51	12:47:03.2	24.12	2.397	NV	CIV	HeII	CIII]
Q2346	BX445	23:48:13.20	00:25:15.8	23.66	2.330	NV	CIV	HeII	CIII]

<sup>a</sup> Emission-line redshift, as measured from the Ly $\alpha$  feature.

<sup>b</sup> The feature of interest was not covered by the LRIS spectral range, indicated as “n.c.”

<sup>c</sup> The feature of interest was covered by the LRIS spectral range but not significantly detected.

<sup>d</sup> A sky line coincides with the wavelength of CIV.

sented here serves as a follow-up to the one described in Steidel et al. (2002), now including BM/BX and additional MD objects, doubling the number of discovered AGN. The normalized redshift distributions for the AGN and non-AGN samples are shown in Figure 1. The average redshift of the 33 AGNs is  $\langle z \rangle = 2.55 \pm 0.31$ , with an average  $\mathcal{R}$  magnitude of  $\langle \mathcal{R} \rangle = 24.2 \pm 0.7$  (a range in  $\mathcal{R}$  of 22.55 – 25.72). For the sample of non-AGNs, reflecting the combined C, D, M, MD, BX, and BM selection windows, the average redshift is  $\langle z \rangle = 2.49 \pm 0.59$ , with an average  $\mathcal{R}$  magnitude of  $\langle \mathcal{R} \rangle = 24.4 \pm 0.6$  (a range in  $\mathcal{R}$  of 21.66 – 25.97<sup>3</sup>). Within the AGN sample, there are 2 BM objects, 13 BX, 9 MD, 4 C, 4 D, and 1 M. These represent  $\sim 1 - 2\%$  of each photometric class within the parent spectroscopic sample. The full sample is listed in Table 1.

When considering the demographics and space density of our sample of AGNs, it is important to consider how their spectroscopic and photometric properties affect their selection, as done for the full sample of non-AGN LBGs in Reddy et al. (2008). To estimate completeness for our sample, we follow the methodology of Steidel et al. (2002), updated for the addition of the  $z \sim 2$  sample. Redshifts were measured for the sample of LBGs by virtue of emission and absorption features

detected in the spectra. The AGN were selected based on the presence of emission lines in addition to Ly $\alpha$ . In order to estimate an upper limit on the number of AGN that would be unrecognized because of low S/N spectra, we examine the strength of the strongest emission line used to infer the existence of an AGN, C IV  $\lambda 1549$ . As discussed above, C IV is, on average,  $\sim 20\%$  the strength of Ly $\alpha$  for the set of 33 AGN spectra. As reported in Steidel et al. (2002), the ratio of C IV to Ly $\alpha$  emission in the  $z \sim 3$  non-AGN LBG sample is  $\leq 1\%$  for the quartile of LBGs having the largest Ly $\alpha$  EW. For the quartile of  $z \sim 2$  non-AGN with the strongest Ly $\alpha$  emission, we measure the ratio of C IV to Ly $\alpha$  flux to be 1% (Dawn Erb, private communication). Given the observed range of Ly $\alpha$  EWs in our sample, we conclude that narrow-lined AGNs would only be found in this strong-Ly $\alpha$  quartile. If we assume that all of the C IV emission in the strong-Ly $\alpha$  composite spectrum is originating from a small sample of undetected AGNs with C IV/Ly $\alpha$  ratios of 20%, then the observed C IV/Ly $\alpha$  ratio of 1% in the strong Ly $\alpha$  composite implies that such objects can only make up 5% of the sample. If we then assume that there are no additional unrecognized AGNs in the other three quartiles with weaker Ly $\alpha$  emission, the fractional contribution of unrecognized AGNs to the full  $z \sim 2$  non-AGN sample is  $\sim 1\%$ . Therefore, our observed frequency of  $\sim 1\%$  of AGN is likely representative of both the spectroscopic

<sup>3</sup> The standard  $\mathcal{R} = 25.5$  limit was relaxed in the Q1422 field.

and photometric samples of UV-selected  $z \sim 2 - 3$  galaxies.

The AGNs presented here are first identified as high-redshift galaxies based on their location in  $U - G$  vs.  $G - \mathcal{R}$  color-color space. Given that the average rest-frame Ly $\alpha$  emission EW for the AGN sample is  $\langle W_{Ly\alpha} \rangle = 80 \text{ \AA}$ , we must consider the effect of Ly $\alpha$  emission on the selection of these objects as a function of redshift. Within certain redshift ranges, Ly $\alpha$  can contribute flux to either the  $U$  or  $G$  bands and alter the position of an AGN in color-color space such that it scatters into or out of the UV-selected sample. For 19 out of 33 AGNs in our sample at  $2.17 \leq z \leq 2.48$  the Ly $\alpha$  feature does not fall within either the  $U$  or  $G$  band, and therefore Ly $\alpha$  emission contributions are irrelevant. One of these objects, HDF-BMZ1156, has anomalously strong C IV emission, which has a significant impact on the observed broadband rest-frame UV colors. For the remaining AGNs (1 object at  $z \leq 2.17$ , and 11 at  $2.48 \leq z \leq 3.40$ ), we investigate how Ly $\alpha$  emission affects their inclusion in the UV-selected sample. Using the measured Ly $\alpha$  EW for each object, we correct the  $U$  or  $G$  band magnitude for Ly $\alpha$  flux as needed in order to characterize the broadband colors in the absence of line emission. This analysis reveals that only 4 out of 12 objects were actually scattered into the selection windows due to the presence of Ly $\alpha$  emission. HDF-BMZ1156 was scattered into the selection window due to its C IV emission. In summary, only 5 out of our 33 AGNs have broadband colors that fail to satisfy the  $UG\mathcal{R}$  selection criteria if not for the presence of strong line emission in the  $U$  or  $G$  filter. On the other hand, the presence of strong Ly $\alpha$  emission may also cause objects to scatter out of the high-redshift galaxy color selection windows. For example, the average Ly $\alpha$  EW of the AGN sample represents a shift of  $\Delta G = 0.26$  magnitudes for an object at  $z = 2.7$  (and a comparable shift in the  $U$  band magnitude for an object at  $z = 2.0$ ). Therefore, objects at  $z > 2.48$  with Ly $\alpha$  emission EWs of this strength will not be identified as high-redshift star-forming galaxies if their line-free  $G - \mathcal{R}$  color is within  $\Delta G$  of the blue  $G - \mathcal{R}$  edge of the color selection box. For a robust comparison of the rest-frame UV continuum and emission-line properties of UV-selected AGNs and non-AGNs, the issues of completeness in color-color space as a result of strong line emission are critical. Because emission lines do not significantly affect the  $U$  and  $G$  magnitudes of UV-selected AGNs at  $2.17 \leq z \leq 2.48$ , these objects serve as a powerful control sample when we compare the rest-frame UV properties of AGNs and non-AGNs in the following sections.

The AGN spectra were obtained with the LRIS spectrograph at the W.M. Keck Observatory (Oke et al. 1995), using multi-object slitmasks with either  $1''.4$  or  $1''.2$  slits. The majority of the spectra in our sample were obtained with either a  $300 \text{ line mm}^{-1}$  grating blazed at  $5000 \text{ \AA}$  or, following the installation of the blue channel of the LRIS instrument, a  $400 \text{ groove mm}^{-1}$  grism blazed at  $3400 \text{ \AA}$ . Additionally, a small number of spectra were obtained with the  $600 \text{ groove mm}^{-1}$  grism blazed at  $4000 \text{ \AA}$ . We refer readers to Steidel et al. (2003, 2004) for a full discussion of the reduction procedures for these data.

### 3. GENERATING THE COMPOSITE SPECTRUM

The current sample of narrow-lined UV-selected AGNs is more than twice as large as the one presented in Steidel et al. (2002). Therefore, the resulting composite spectrum of these objects enables the identification of weak emission and absorption lines not visible in the average of the previous smaller sample. To create the composite spectrum, we took the individual extracted, one-dimensional, flux-calibrated AGN spectra from our sample, and shifted them to the rest frame as described below. The spectra were scaled to a common median in the wavelength range of  $1250 - 1380 \text{ \AA}$  and then averaged. To exclude positive and negative sky subtraction residuals, we rejected the four highest and lowest outliers at each wavelength of the composite spectrum, which corresponded to  $\sim 20\%$  of the data. Composite spectra constructed from the median of the flux values at each wavelength yielded results indistinguishable from those based on composite spectra constructed from the average of the flux values.

In order to construct the composite spectrum, each individual spectrum was shifted to the rest frame, which requires an accurate measurement of the galaxy's systemic redshift. The establishment of an accurate systemic redshift is also necessary for estimating the absolute values of kinematic offsets for different interstellar components in the composite spectrum. The low S/N of the AGN spectra only allows for a measurement of the strongest rest-frame UV features, such as the emission lines H I Ly $\alpha$ , N V  $\lambda 1240$ , C IV  $\lambda 1549$ , He II  $\lambda 1640$ , and C III]  $\lambda \lambda 1907, 1909$ . Absorption features were not detected in enough spectra to be used to calculate redshifts. The spectra for all of our 33 objects contain a Ly $\alpha$  emission feature. However, it is well known that Ly $\alpha$  is not a reliable indicator of the stellar redshift of a galaxy due to resonant scattering of the line (Pettini et al. 2001; Shapley et al. 2003; Adelberger et al. 2003; Steidel et al. 2010), therefore we consider the emission lines associated with AGN activity. As indicated in Table 1, N V  $\lambda 1240$ , C IV  $\lambda 1549$ , He II  $\lambda 1640$ , and C III]  $\lambda \lambda 1907, 1909$  were detected in many individual spectra. However, many of these detections do not have the signal-to-noise necessary to calculate an accurate redshift. Furthermore, C III]  $\lambda \lambda 1907, 1909$  is a density-sensitive doublet whose blended centroid varies as a function of density, so this feature is also unsuitable for measuring redshifts. In general, C IV and He II were the two emission features that yielded the highest signal-to-noise detections in the individual spectra. We measure accurate centroids for C IV in 19 of our 33 objects, and He II in 17 of our 33 objects. We calculated how the redshifts derived from C IV  $\lambda 1549$  and He II  $\lambda 1640$  compared to the Ly $\alpha$  redshifts. The average (median) difference in velocity between Ly $\alpha$  and C IV  $\lambda 1549$ , is  $\Delta v = -7 \text{ km s}^{-1}$  ( $24 \text{ km s}^{-1}$ ), where a negative [positive] velocity difference indicates blueshift [redshift]. It has previously been shown that the velocities traced by the Ly $\alpha$  and C IV emission lines agree in active galaxies (Buson & Ulrich 1990). However, the average (median) difference in velocity between Ly $\alpha$  and He II  $\lambda 1640$  is  $\Delta v = 173 \text{ km s}^{-1}$  ( $169 \text{ km s}^{-1}$ ). As He II  $\lambda 1640$  is not a resonance line, it serves as a better tracer for the redshift of the stars in the galaxy than either Ly $\alpha$  or C IV  $\lambda 1549$ , which are subject to radiative transfer effects (Villar-Martín et al. 2000, 2003).

In the absence of stellar absorption lines, H $\alpha$  is used in

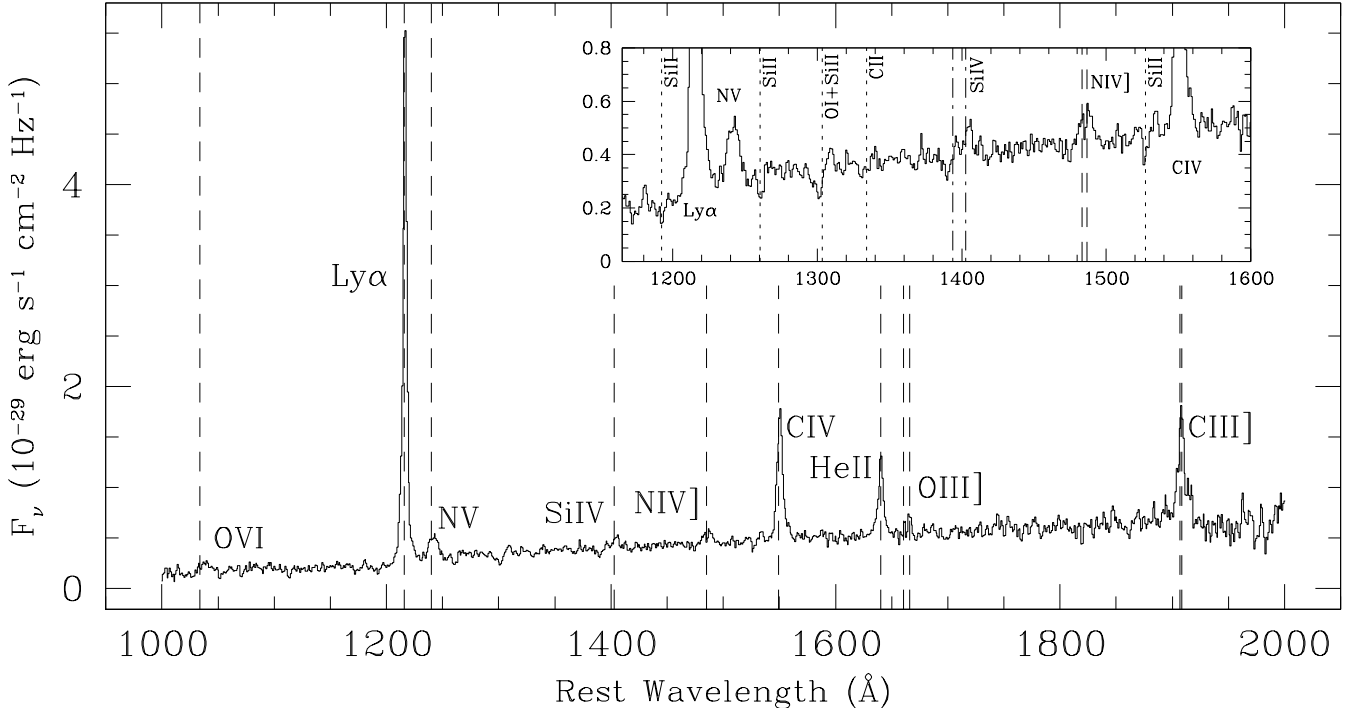


FIG. 2.— The composite rest-frame UV spectrum for 33 narrow-lined AGN at  $z \sim 2 - 3$ . These objects were selected by virtue of their emission lines, such as N V  $\lambda 1240$ , C IV  $\lambda 1549$ , and He II  $\lambda 1640$ . The dashed lines indicate the locations of emission lines, while the inset highlights some of the more prominent absorption features. Dotted lines are used to mark low-ionization absorption features, and dot-dashed lines indicate high-ionization absorption features.

the rest-frame optical to derive redshifts. We compared the redshifts derived from optical spectra for five AGN from our sample taken with the NIRSPEC instrument on the Keck II telescope (McLean et al. 1998). For these objects, the average (median) velocity difference between Ly $\alpha$  and H $\alpha$  is  $\Delta v = 132 \text{ km s}^{-1}$  ( $208 \text{ km s}^{-1}$ ), while the average (median) difference between He II  $\lambda 1640$  and H $\alpha$  is  $\Delta v = -37 \text{ km s}^{-1}$  ( $59 \text{ km s}^{-1}$ ). With this in mind, the average velocity difference between Ly $\alpha$  and He II  $\lambda 1640$ , for composite spectra created with only those objects where both lines were detected in the spectrum, is  $-196 \pm 50 \text{ km s}^{-1}$ . We adopted this Ly $\alpha$ -He II offset for all of the objects in the sample, and added it to each Ly $\alpha$  redshift to estimate the systemic redshift for each object. We note that the composite spectrum is virtually identical if individual He II redshifts are used to estimate the rest frame for the objects with robust He II centroid measurements, as opposed to the average Ly $\alpha$ -He II offset. Furthermore, a stack of the 16 spectra without individual He II centroid measurements, using the average Ly $\alpha$ -He II offset to estimate the rest frame, results in a He II profile centered at zero velocity. These consistency checks indicate the validity of adopting the average Ly $\alpha$ -He II offset for all spectra in order to estimate the rest frame.

#### 4. FEATURES IN THE COMPOSITE SPECTRUM

The final composite spectrum is shown in Figure 2, an average of the spectra for our 33 AGNs. We identify several nebular emission lines, including N V  $\lambda 1240$ , C IV  $\lambda 1549$ , He II  $\lambda 1640$ , and C III]  $\lambda \lambda 1907, 1909$ . We also detect N IV]  $\lambda 1486$ , which has previously been detected locally in compact planetary nebulae (Davidson et al. 1986), at  $z = 3.4$  in the Lynx arc (Fosbury et al. 2003),

in high-redshift QSOs (Bentz et al. 2004; Glikman et al. 2007), in a  $z = 5.563$  Ly $\alpha$  emitter (Vanzella et al. 2009; Raiter et al. 2010), and in radio galaxies (Vernet et al. 2001; Humphrey et al. 2008). We also detect absorption features shown in the inset of Figure 2. Many of these are observed in the LBG non-AGN composite spectrum from Shapley et al. (2003), including the low-ionization lines, Si II  $\lambda 1260$ , O I  $\lambda 1302 + \text{Si II } \lambda 1304$ , Si II  $\lambda 1527$ , and high-ionization feature, Si IV  $\lambda \lambda 1393, 1402$ .

We measured the rest-frame centroids (and corresponding relative velocities), EWs, and FWHM values for each of the emission lines and absorption lines, which are found in Tables 2 and 3. Gaussian profiles were fit to the measured spectroscopic features to estimate line centroids. These centroids were then used to estimate velocities relative to the systemic frame. In cases where the lines are a blend of two closely spaced emission or absorption features, a rest-frame blend value was calculated based on the oscillator strengths for the pair and used to estimate the velocity. The EW was calculated by first measuring the values of the continuum on either side of the line of interest, integrating the flux in the line between these points, and then dividing the flux by the average of the continuum values.

##### 4.1. Uncertainties

The measurements from the composite spectrum are only meaningful if accompanied by an analysis of the associated errors. The uncertainty on the EW values for the composite spectrum is dependent on both the range of EW of the individual sample galaxies as well as the finite S/N of the composite spectrum. Almost all but the strongest features cannot be measured in individual spectra.

TABLE 2  
 ABSORPTION FEATURES

Ion	$\lambda_{\text{lab}}^a$ (Å)	$\lambda_{\text{blend}}^a$ (Å)	$\lambda_{\text{obs}}^b$ (Å)	$W_0^c$ (Å)	$\Delta v^d$ (km s <sup>-1</sup> )
SiII <sup>e</sup>	1190.42, 1193.28	1192.33	1191.84±1.32	-1.70±0.68	-123±333
SiII <sup>e</sup>	1260.42	-	1260.45±0.94	-2.51±0.55	7±223
OI + SiII <sup>e</sup>	1302.17, 1304.37	1303.27	1300.37±0.94	-2.11±0.34	-667±216
SiIV <sup>f</sup>	1393.76	-	1389.83±0.83	-1.18±0.44	-845±178
SiII <sup>e</sup>	1526.7	-	1526.49±1.00	-0.73±0.27	-41±197

<sup>a</sup> Vacuum wavelength.

<sup>b</sup> Observed wavelength.

<sup>c</sup> Rest-frame EW and  $1\sigma$  error. The error takes into account both sample variance and the S/N of the composite spectrum (see §4.1).

<sup>d</sup> Relative velocity measured in the systemic rest frame of the composite spectrum, equivalent to the rest frame of the stars.

<sup>e</sup> Low-ionization absorption feature.

<sup>f</sup> High-ionization absorption feature.

 TABLE 3  
 EMISSION FEATURES

Ion	$\lambda_{\text{lab}}^a$ (Å)	$\lambda_{\text{blend}}^a$ (Å)	$\lambda_{\text{obs}}^b$ (Å)	$W_0^c$ (Å)	$\Delta v^d$ (km s <sup>-1</sup> )
OVI	1031.912, 1037.613	1033.82	1037.94±2.20	6.01±2.20	1196±639
Ly $\alpha$	1215.67	-	1216.47±0.04	66.39±11.65	197±10
NV	1238.821, 1242.804	1240.15	1242.09±0.64	5.60±1.00	470±154
SiII* <sup>e</sup>	1309.276	-	1309.22±0.54	0.63±0.24	-13±124
SiIV	1402.77	-	1405.02±0.93	1.44±0.58	481±176
NIV]	1483.321, 1486.496	- <sup>d</sup>	1486.59±1.17	2.00±0.78	
CIV	1548.202, 1550.774	1549.06	1550.47±0.38	16.34±2.86	273±74
HeII	1640.405	-	1640.45±0.27	8.07±1.32	8±50
OIII]	1660.809	-	1661.63±1.28	0.32±1.32	148±231
OIII]	1666.150	-	1666.09±0.65	1.10±0.39	-10±118
CIII]	1906.683, 1908.734	- <sup>d</sup>	1908.28±0.80	13.96±4.20	

<sup>a</sup> Vacuum wavelength.

<sup>b</sup> Observed wavelength.

<sup>c</sup> Rest-frame EW and  $1\sigma$  error. The error takes into account both sample variance and the S/N of the composite spectrum (see §4.1).

<sup>d</sup> Relative velocity measured in the systemic rest frame of the composite spectrum, equivalent to the rest frame of the stars. Relative velocities were not calculated for the density-sensitive N IV] and C III] doublets, for which the blend wavelength depends on the uncertain electron density.

<sup>e</sup> The asterisk indicates that this feature is a fine-structure emission line.

To reflect sample variance and also statistical noise, we used a bootstrap technique outlined in Shapley et al. (2003) to calculate the uncertainties. In this method, we generated 500 fake composite spectra constructed from the sample of spectra used in creating the real composite spectra. Each fake spectrum was constructed in the same way, with the same number of spectra as the actual composite, but with the list of input spectra formulated by selecting spectra at random, with replacement, from the full list of AGN spectra ( $\sim 36\%$  of sample is replaced by duplicates). With these 500 fake spectra, we measured the line centroids (and velocities) and EWs for all of the emission and absorption features detected in the original composite spectrum. The standard deviation of the 500 individual measurements represents the errors on these values.

#### 4.2. Emission Features

The emission features for the full composite spectrum are shown in Table 3. The most prominent feature is Ly $\alpha$ , which, for the individual AGN spectra, is always

observed in emission. In Shapley et al. (2003), the Ly $\alpha$  feature was detected both in emission and absorption for a sample of 820 non-AGN LBGs. We measure a  $\Delta v = +197$  km s<sup>-1</sup> emission redshift from our composite spectrum, which is slightly lower, but similar to what is observed in the non-AGN LBG sample ( $\Delta v = +360$  km s<sup>-1</sup>). This redshift is due to the scattering of Ly $\alpha$  photons off of redshifted material in the galaxy, which allows the (now off-resonance) photons to escape. The measured EW is  $W_{\text{Ly}\alpha} = 66$  Å, which is similar to the EW measured from the quartile of non-AGN objects from Shapley et al. (2003) with the strongest Ly $\alpha$  EW.

The other strong emission lines we see in the composite spectrum are N V  $\lambda 1240$  ( $W_{\text{N V}} = 5.6$  Å), C IV  $\lambda 1549$  ( $W_{\text{C IV}} = 16.3$  Å), He II  $\lambda 1640$  ( $W_{\text{He II}} = 8.1$  Å), and C III]  $\lambda\lambda 1907, 1909$  ( $W_{\text{C III]}} = 14.0$  Å). The majority of non-AGN LBGs do not show evidence for these features with such large EW values, even in those LBGs with strong Ly $\alpha$  emission (Shapley et al. 2003). Both N V and C IV have redshifts that are similar to the one measured for Ly $\alpha$ . Because we are using a composite spectrum,

which has a higher S/N ratio than the individual spectra, we can detect weaker emission lines as well. We detect N IV]  $\lambda$ 1486, as well as O VI  $\lambda\lambda$ 1032, 1038, and O III]  $\lambda\lambda$ 1661, 1666. As mentioned in §2, while the EW values of Ly $\alpha$  are similar between the non-AGN and the AGN composite spectra, the strongest emission line indicative of an AGN in the non-AGN spectra is C IV  $\lambda$ 1549, which is only seen at 1% the strength of Ly $\alpha$ .

The ratios of strong UV emission lines have been used to understand the underlying shock and photoionization conditions in the gas. Ly $\alpha$  is generally not used for diagnostic purposes because of the resonance scattering and the effects of strong dust attenuation on this line. The ratios of C IV  $\lambda$ 1549/C III]  $\lambda$ 1909, C IV  $\lambda$ 1549/He II  $\lambda$ 1640, and C III]  $\lambda$ 1909/He II  $\lambda$ 1640 can be used to discriminate between shock and photoionization predictions for narrow emission-line regions in AGNs (Villar-Martin et al. 1997; Allen et al. 1998; Groves et al. 2004). For the full composite spectrum we measure values of the ratios of these lines that are very similar to the range of observed ratios in high-redshift radio galaxies (Villar-Martin et al. 1997; Nagao et al. 2006a; Matsuoka et al. 2009).

#### 4.3. Absorption Features

In addition to the strong emission lines seen in the composite spectrum, we detect several weak interstellar absorption features as well, such as the low-ionization lines Si II  $\lambda$ 1260, O I  $\lambda$ 1302+Si II  $\lambda$ 1304, and Si II  $\lambda$ 1527. We do not detect C II  $\lambda$ 1334 in our composite spectrum, which is a low-ionization absorption feature detected in the non-AGN composite spectrum from Shapley et al. (2003)<sup>4</sup>. The origin of this difference requires further study. The unblended low-ionization lines detected do not show significant blueshifts, in contrast to the blueshifts of  $\sim 150 - 200 \text{ km s}^{-1}$  observed in the non-AGN sample (Shapley et al. 2003; Steidel et al. 2004, 2010). This conclusion is dependent on our definition of the rest frame for the individual spectra. As discussed in §3, our method uses the centroid of He II  $\lambda$ 1640 emission as a proxy for the rest frame. On the other hand, the rest frame for the spectra included in the non-AGN LBG composite from Shapley et al. (2003) was established using average relationships between the centroids of rest-frame optical nebular emission lines and those of rest-frame UV features, such as interstellar absorption lines and Ly $\alpha$  emission (Adelberger et al. 2003). Below we discuss how a change in the rest-frame determination would affect our conclusions about interstellar absorption line kinematics. However, we note that, regardless of the rest-frame determination, the observed offset between Ly $\alpha$  emission and low-ionization interstellar absorption lines in the AGN composite spectrum ( $\sim 200 \text{ km s}^{-1}$ ) is significantly smaller than the corresponding offset observed in the non-AGN composite ( $\sim 510 \text{ km s}^{-1}$ ) – indicating an intrinsic difference in kinematics traced by low-ionization gas. While the observed centroid of O I  $\lambda$ 1302+Si II  $\lambda$ 1304 may indicate a blueshift, it is most likely contaminated by additional absorption at 1296 Å. This absorption may be due to the stellar feature Si III  $\lambda$ 1296 (Chandar et al. 2005), but higher signal-to-noise

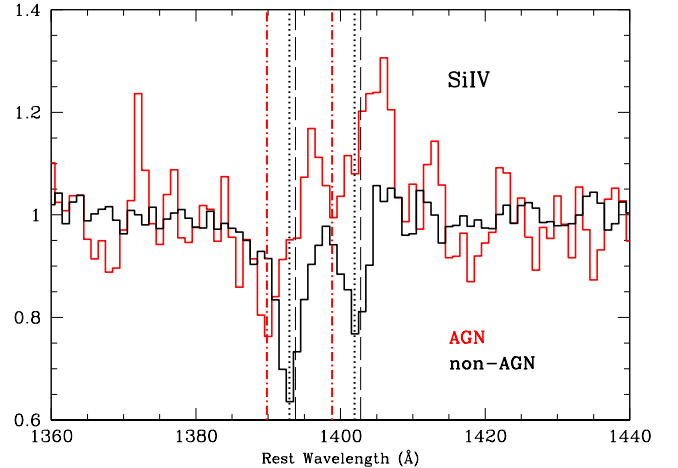


FIG. 3.— Comparison of the blueshift of the Si IV  $\lambda$ 1393 and  $\lambda$ 1402 line between the continuum normalized AGN composite spectrum (in red) and the non-AGN composite spectrum (in black) presented in Shapley et al. (2003). The long dashed lines mark the rest-frame wavelengths of both Si IV  $\lambda$ 1393 and  $\lambda$ 1402, while the dotted and dot-dashed lines show the measured blueshifted centroids for the non-AGN and AGN composite spectra, respectively. The measured centroid of the Si IV  $\lambda$ 1393 feature indicates a velocity offset of  $-845 \pm 171 \text{ km s}^{-1}$  in the AGN composite spectrum, while in the non-AGN spectrum, it is  $-180 \text{ km s}^{-1}$ . Although it is difficult to determine robustly the full Si IV absorption profile in the AGN composite spectrum due to contamination by Si IV emission, we emphasize differences in the blue wing of the  $\lambda$ 1393 absorption feature. There is excess absorption at the most blueshifted velocities in the AGN composite relative to that of the non-AGNs.

spectra will be required to confirm this possibility.

We also detect the high-ionization feature Si IV  $\lambda\lambda$ 1393, 1402, both in emission and absorption. We use the stronger Si IV  $\lambda$ 1393 feature as a probe of absorption line kinematics. This feature is resolved, with a FWHM greater than  $500 \text{ km s}^{-1}$ . The Si IV centroid indicates a significant blueshift,  $-845 \pm 178 \text{ km s}^{-1}$ , which is several times larger than the one measured in the non-AGN composite spectrum ( $\Delta v = -180 \text{ km s}^{-1}$ ). This difference is demonstrated in Figure 3, which shows both the AGN composite spectrum described here and the non-AGN composite from Shapley et al. (2003), zoomed in on the region around Si IV. One potential cause for concern is the contamination of Si IV absorption profiles by the corresponding Si IV emission lines, given their close proximity in wavelength. The Si IV  $\lambda$ 1393 emission line is in fact measured to be narrower than the  $\lambda$ 1402 feature, suggesting that its blue edge is attenuated by Si IV  $\lambda$ 1393 absorption, which is stronger than absorption from Si IV  $\lambda$ 1402. Furthermore, the Si IV  $\lambda$ 1393 emission feature is observed to be weaker than that of Si IV  $\lambda$ 1402, while the relative oscillator strengths of the doublet members suggest that Si IV  $\lambda$ 1393 should be twice as strong as  $\lambda$ 1402. Both of these observations indicate the possible blending of Si IV emission and absorption.

In order to quantify the contamination from emission in the observed Si IV  $\lambda$ 1393 absorption profile, we require a robust model of the intrinsic Si IV  $\lambda$ 1393 emission. Such a model is not straightforward to construct, given that both Si IV  $\lambda$ 1393 and  $\lambda$ 1402 emission features are affected by absorption, and, furthermore, the Si IV  $\lambda$ 1402 emission feature is blended with emission from O IV]  $\lambda$ 1401. The ratio between O IV]  $\lambda$ 1401 and

<sup>4</sup> While not detected in the full composite spectrum, C II  $\lambda$ 1334 is marginally detected in four of the individual spectra, HDF-BX160, Q0000-C14, Q0100-BX172, and Q1700-MD157.

Si IV  $\lambda 1402$  is not well constrained, but can exceed unity (Hamann et al. 2002; Nagao et al. 2006b), in which case the inferred Si IV  $\lambda 1393$  would be much weaker than if all the emission at  $\sim 1402$  Å was due to Si IV. While the potential contamination from Si IV emission prevents us from tracing out the full Si IV absorption profile, we can still assert that absorbing gas exists at a blueshift with a magnitude of  $845 \text{ km s}^{-1}$ . Furthermore, as shown in Figure 3, this highly blueshifted gas in the AGN composite spectrum at  $\sim -1000 \text{ km s}^{-1}$  does not have a corresponding component in the non-AGN composite spectrum, representing a quantitative difference between the velocity profiles of outflowing absorbing gas in the two samples. Here we return to the issue of the discrepancy between the low-ionization Si II absorption-line blueshift measured in the AGN and non-AGN LBG composite spectra. The non-AGN LBG composite spectrum has low-ionization Si II absorption lines blueshifted by  $\sim 150 - 200 \text{ km s}^{-1}$ , while the Si II absorption in the AGN composite spectrum does not show the same blueshift. If this difference were due to systematics of the rest-frame determinations, and we instead forced the Si II absorption lines in the AGN composite to have the same blueshifts as those in the non-AGN composite, the blueshift of Si IV would *increase* to  $\geq 1000 \text{ km s}^{-1}$ .

#### 4.4. Continuum Shape

Besides the emission and absorption features seen in the composite spectrum, the shape of the underlying continuum can be used to discern the presence of dust in these objects. The continuum shape is often described by  $\beta$ , the slope of a power law of the form  $F_\lambda \propto \lambda^\beta$  fit to the continuum. We used a modified version of the method outlined in Calzetti et al. (1994), using windows of the continuum with little to no activity as anchor points for fitting the power law. For the full composite spectrum, we measured  $\beta = -0.314$ , while for the full non-AGN LBG composite from Shapley et al. (2003), we measured  $\beta = -1.49$ , which is significantly bluer. A comparison between AGN and non-AGN composite spectra is shown in Figure 4. We note here that in a composite spectrum of the control sample of objects at  $2.17 \leq z \leq 2.48$ , for which Ly $\alpha$  emission does not affect the UGR photometry, the UV slope is at least as red as in the composite spectrum for our full AGN sample. This result demonstrates that the red UV continuum slope measured for our AGN sample does not simply arise from red objects, which wouldn't satisfy the rest-frame UV selection criteria otherwise, scattering into the UV selection box due to the presence of strong Ly $\alpha$  emission. A full interpretation of the red AGN continuum awaits detailed population synthesis modeling which will be presented in Hainline et al. (in preparation), yet preliminary analysis suggests the AGN continuum does not contribute significantly at rest-frame UV wavelengths (Assef et al. 2009).

Aird et al. (2010) argue that the redder rest-frame UV continuum slopes of UV-selected narrow lined AGNs relative to star-forming galaxies can result in a reduced overall selection efficiency in color-color space. However, these authors do not take into account the simultaneous effects of continuum shape and strong emission lines in calculating the AGN selection efficiency, which can have a significant impact on the colors of narrow-

lined AGNs in certain redshift ranges (as discussed in §2). Our main conclusions about rest-frame UV spectroscopic trends within the UV-selected narrow-lined AGN sample are not significantly affected by these considerations. If anything, the difference we report between AGN and non-AGN continuum slope would be increased by including the spectra of red AGNs that do not fall in the color selection box due to their  $G - \mathcal{R}$  colors.

#### 5. AGN SPECTROSCOPIC TRENDS

In order to discern spectroscopic trends in the AGN sample, we split the objects into various subsamples based on the properties of the individual spectra. Given the relatively small sample size (33 objects) and our desire to maximize the S/N of the resulting subsample composite spectra, we simply divide the sample in half for these analyses. The properties used to divide our sample include: Ly $\alpha$  emission line EW, rest-frame UV absolute magnitude, and redshift. We do not split our sample by the EW for any of the other emission or absorption lines because most of our spectra do not have high enough S/N to allow for robust measurements of these features. The results for measuring various properties from the composite spectra described in this section are found in Table 4.

##### 5.1. Ly $\alpha$ Dependencies

Ly $\alpha$  is detected in emission in all of our AGN, with EW values that range from  $W_{\text{Ly}\alpha} = 10 \text{ \AA}$  to  $W_{\text{Ly}\alpha} = 300 \text{ \AA}$ . In contrast, the non-AGNs show Ly $\alpha$  both in emission and absorption. The median value for the Ly $\alpha$  EW in our sample was  $W_{\text{Ly}\alpha} = 63 \text{ \AA}$ , which is where we split the sample, creating a composite spectrum for those spectra with  $W_{\text{Ly}\alpha} < 63 \text{ \AA}$  and those with  $W_{\text{Ly}\alpha} > 63 \text{ \AA}$ . The results of measuring the various properties of the composite spectra are found in Table 4. The measured Ly $\alpha$  EW in the strong Ly $\alpha$  composite spectrum is  $W_{\text{Ly}\alpha, \text{strong}} = 123 \pm 14 \text{ \AA}$ , which is almost five times larger than what is measured in the weak Ly $\alpha$  composite spectrum,  $W_{\text{Ly}\alpha, \text{weak}} = 28 \pm 5 \text{ \AA}$ . The Ly $\alpha$  EWs measured from the composite spectra are consistent with the sample mean values of  $\langle W_{\text{Ly}\alpha, \text{strong}} \rangle = 141 \pm 15 \text{ \AA}$  and  $\langle W_{\text{Ly}\alpha, \text{weak}} \rangle = 33 \pm 4 \text{ \AA}$ .

The strong Ly $\alpha$  composite spectrum has significantly larger C IV, He II, and C III] EW values than the spectrum with weaker Ly $\alpha$  emission, but only by a factor of two. The same trend is observed when we consider line fluxes as opposed to equivalent widths. For both equivalent widths and fluxes, the change in Ly $\alpha$  is not accompanied by an equivalent change in the strength of emission lines that are primarily sensitive to the level of nuclear activity.

In the strong Ly $\alpha$  EW composite spectrum, most low-ionization (Si II  $\lambda 1260$ , C II  $\lambda 1334$ , and Si II  $\lambda 1527$ ) and high-ionization (Si IV  $\lambda \lambda 1393, 1402$ ) absorption lines are statistically weaker than the features measured in the weak Ly $\alpha$  EW composite spectrum. This difference is shown in Figure 5, which overplots the strong and weak Ly $\alpha$  EW composite spectra. This trend of absorption line strength being anticorrelated with Ly $\alpha$  EW is also seen in the non-AGN LBGs (Shapley et al. 2003). The O I  $\lambda 1302$ +Si II  $\lambda 1304$  absorption line, however, is of a similar strength in both spectra. The potential contamination by Si III  $\lambda 1296$  discussed in Section 4.3 is

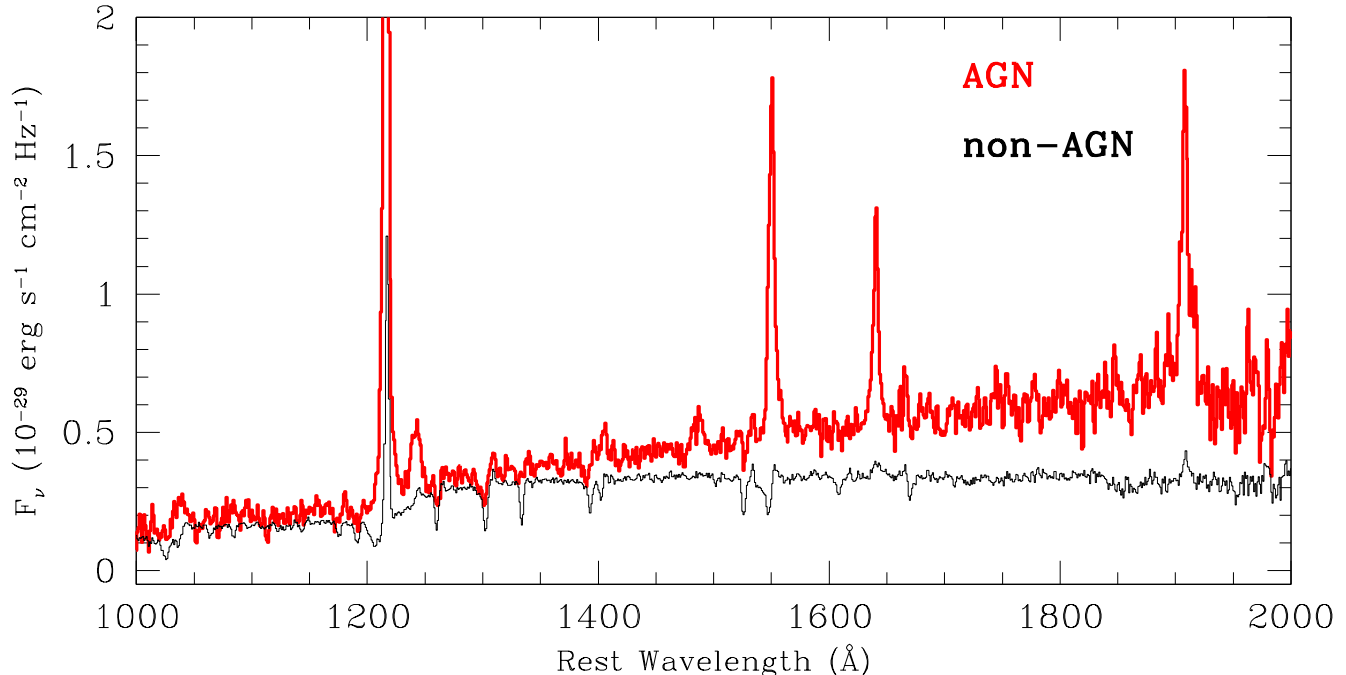


FIG. 4.— Comparison of the continuum slope between the AGN composite spectrum and the non-AGN composite spectrum from Shapley et al. (2003). The AGN composite is significantly redder than the non-AGN composite. The power law slope  $\beta$ , as measured directly from the AGN spectrum, is  $\beta = -0.314$ , while for the non-AGN spectrum,  $\beta = -1.49$ .

more prominent in the strong Ly $\alpha$  EW composite, while it is not seen in the weak Ly $\alpha$  EW composite. In the weak Ly $\alpha$  EW composite, the O I+Si II feature has a much smaller offset than what is seen in the full composite spectrum. Finally, C II is detected in the weak Ly $\alpha$  spectrum while not present in either the strong Ly $\alpha$  or full composite spectra (see §4.3). Beyond the trends in emission and absorption line strength, the two binned spectra do not differ in many other respects. They are not statistically different in UV luminosity or continuum color.

### 5.2. UV Magnitude Dependencies

We calculated the UV magnitude for each of our galaxies using the value for a galaxy’s redshift to interpolate the flux at 1500 Å from the  $G - R$  color. With this flux, we calculated a UV luminosity and AB magnitude for each object. The normalized UV magnitude distributions for the AGN and non-AGN samples are shown in Figure 6. The median magnitude is  $M_{UV,AB} = -20.7$ , so we split the sample into  $M_{UV,bright}$  and  $M_{UV,faint}$  subsamples for making composite spectra.

The resulting spectra have Ly $\alpha$  EWs that are statistically similar, while the  $M_{UV,faint}$  sample has overall weaker interstellar absorption lines. This difference in interstellar absorption line strength is not as significant as the one observed between the two Ly $\alpha$  composite spectra described in §5.1, indicating a stronger connection between Ly $\alpha$  emission strength and interstellar absorption strength, as observed in non-AGN LBGs (Shapley et al. 2003). Additionally, the two spectra separated by  $M_{UV}$  are quite different in continuum color. The  $M_{UV,bright}$  composite spectrum is significantly bluer ( $\beta_{spec} = -0.67$ ) than the  $M_{UV,faint}$  composite ( $\beta_{spec} = -0.06$ ), yet both are redder than non-AGN LBG composite ( $\beta_{spec} = -1.49$ ). The average line flux for AGN-

sensitive features such as C IV, He II, and C III] is larger in the  $M_{UV,bright}$  composite than in the  $M_{UV,faint}$  one. If the line fluxes and UV continuum flux density scaled by the same factor, which would indicate a direct connection between nuclear activity and UV continuum emission, the average EWs in the bright and faint composites would also be identical. In fact, the average EWs of the AGN-sensitive features in the  $M_{UV,faint}$  sample are larger than those in the  $M_{UV,bright}$  sample, suggesting that the relationship between AGN-sensitive emission lines and UV continuum is not direct. While this trend is consistent with the trend observed in broad-lined QSOs (Baldwin 1977), as these are narrow-lined AGNs, with only an obscured view of the central engine, we do not expect that the AGN emission contributes to the overall UV continuum (Assef et al. 2009) in either the bright or faint subsample. The difference in emission-line strength may simply indicate the correlation of AGN activity with additional properties of the host galaxy stellar population. Further population synthesis modeling is required to fully characterize these trends.

### 5.3. Redshift Dependencies

We separated the spectra by redshift at  $z = 2.7$ , effectively splitting between the  $z \sim 3$  LBG sample and the newly added  $z \sim 2$  BX/BM and MD objects. There are 9 objects used to generate the  $z > 2.7$  composite, and 24 to generate the  $z < 2.7$  composite. The results for separating the spectra by redshift are very similar to those seen when separating by  $W_{Ly\alpha}$ , with the higher redshift sample showing stronger Ly $\alpha$  emission on average. The Ly $\alpha$  EW distribution for the high redshift sample spans the range of 15 to 300 Å ( $\langle W_{Ly\alpha,z>2.7} \rangle = 124 \pm 28$ ), while the Ly $\alpha$  EW distribution for the low redshift sample spans the range of 10 to 145 Å ( $\langle W_{Ly\alpha,z<2.7} \rangle = 62 \pm 8$ ). Given that strong line emission can affect the selection of these

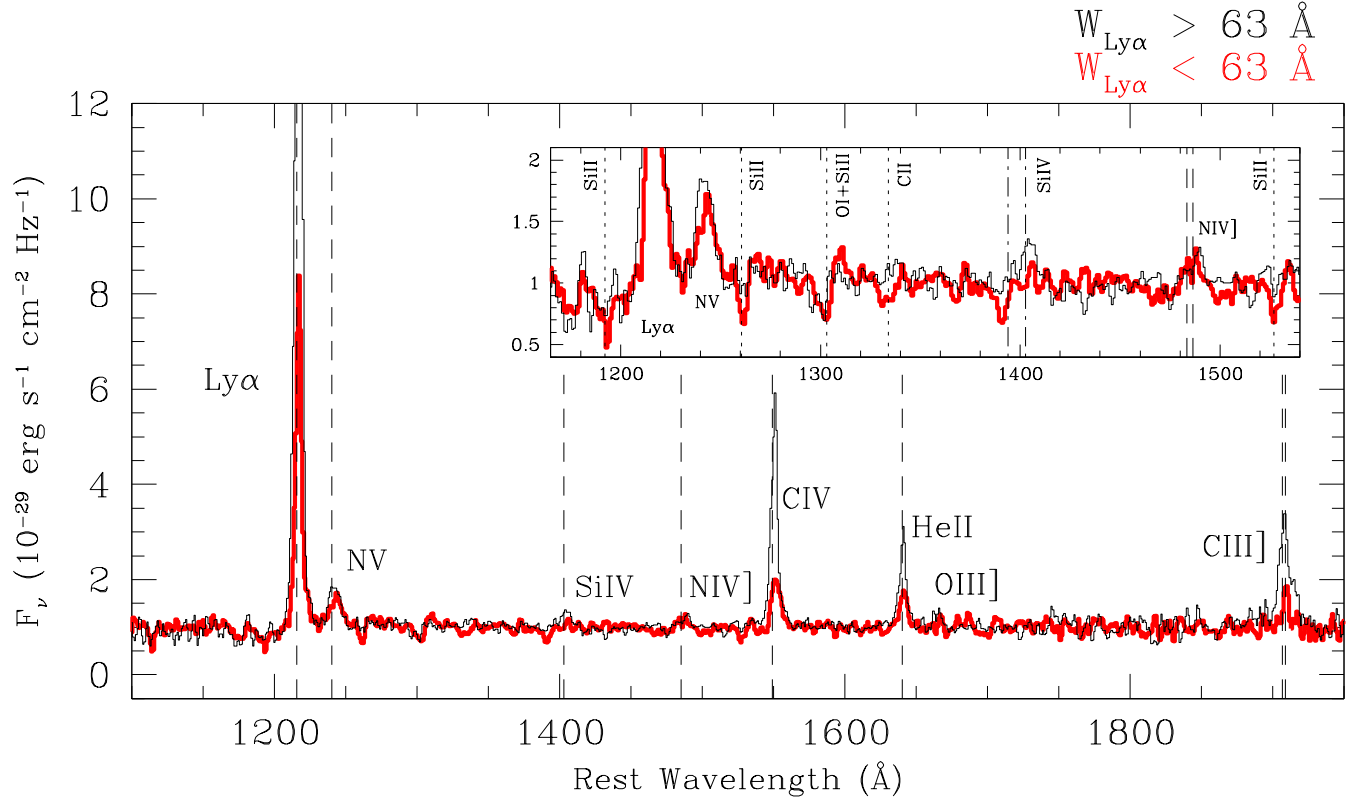


FIG. 5.— Composite spectra of objects separated by  $\text{Ly}\alpha$  EW. Plotted in black is the continuum normalized composite spectrum from the half of galaxies in our AGN sample with the strongest  $\text{Ly}\alpha$  emission, while plotted in red is the continuum normalized composite spectrum from the half of galaxies with the weakest  $\text{Ly}\alpha$  emission. The absorption lines are significantly weaker in the strong  $\text{Ly}\alpha$  composite spectrum, which is consistent with the results from Shapley et al. (2003) for non-AGN LBGs. Dashed lines indicate emission lines, dotted lines indicate low-ionization absorption features, and dot-dashed lines indicate high-ionization absorption lines.

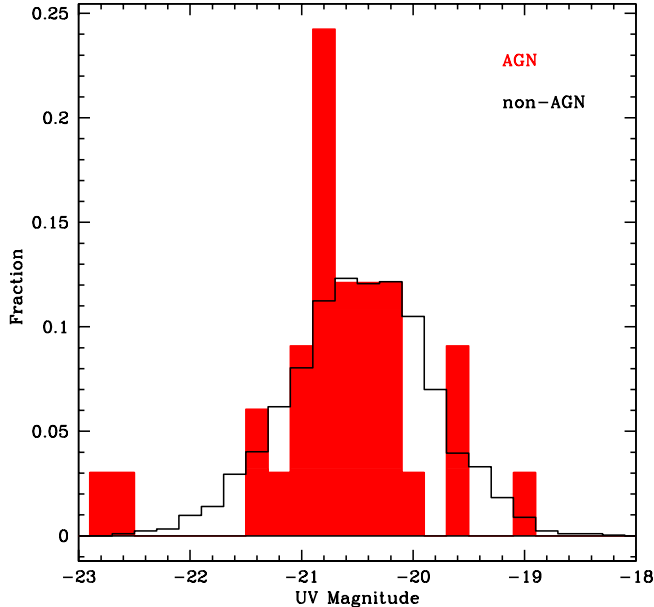


FIG. 6.— The normalized UV absolute magnitude distribution for our sample of UV-selected narrow-lined AGNs, compared to the distribution for the  $z \sim 2-3$  UV-selected non-AGN sample. These UV magnitudes were calculated from the  $G-R$  colors and  $\text{Ly}\alpha$ -derived redshifts for the objects.

objects as a function of redshift, we removed from the analysis the 5 AGNs whose broadband colors only satisfied the  $UGR$  selection criteria because of the presence of  $\text{Ly}\alpha$  or C IV. Even with these objects removed we still find a larger average  $\text{Ly}\alpha$  EW for the higher redshift sample. While these differences are suggestive of redshift evolution in the  $\text{Ly}\alpha$  EW distributions in a similar sense to what is observed in star-forming galaxies over the same redshift range (Reddy et al. 2008; Nilsson et al. 2009), the small sample size precludes us from drawing any firm conclusions.

## 6. DISCUSSION

Analysis of the composite spectrum of the UV-selected AGNs at  $z \sim 2-3$  reveals a number of results regarding the nature of AGN activity. We report the detection of weak absorption lines from both low- and high-ionization species. Most strikingly, the high-ionization Si IV absorption feature exhibits a significant blueshift of  $\Delta v = -845 \pm 178 \text{ km s}^{-1}$ . The precise value of this blueshift is referenced to our estimate of the rest frame based on He II  $\lambda 1640$ . As discussed in §4.3, if we adopt a rest frame in which the low-ionization lines have the same blueshift as those in the non-AGN LBG composite spectrum of Shapley et al. (2003), then the magnitude of the inferred blueshift for Si IV would be even greater. While contamination from Si IV emission prevents us from tracing out the full Si IV velocity profile in absorption, the most strongly blueshifted material appears to be outflowing more rapidly than the associated gas in star-forming

TABLE 4  
 SPECTROSCOPIC PROPERTIES OF COMPOSITE SPECTRUM SUBSAMPLES

	$W_{Ly\alpha} > 63$	$W_{Ly\alpha} < 63$	$M_{UV,bright}$	$M_{UV,faint}$	$z > 2.7$	$z < 2.7$
$N_{gal}$	16	17	16	17	9	24
$\langle z_{Ly\alpha} \rangle^a$	$2.60 \pm 0.08$	$2.49 \pm 0.06$	$2.65 \pm 0.08$	$2.43 \pm 0.05$	$2.94 \pm 0.07$	$2.37 \pm 0.02$
$\langle M_{UV} \rangle^a$	$-20.6 \pm 0.2$	$-20.7 \pm 0.2$	$-21.2 \pm 0.1$	$-20.2 \pm 0.1$	$-21.1 \pm 0.2$	$-20.5 \pm 0.1$
$\langle W_{Ly\alpha} \rangle^a$	$141 \pm 15$	$33 \pm 4$	$78 \pm 14$	$82 \pm 17$	$124 \pm 28$	$62 \pm 8$
$\langle \beta_{G-R} \rangle^a$	$-0.8 \pm 0.2$	$-1.2 \pm 0.1$	$-1.1 \pm 0.2$	$-0.9 \pm 0.2$	$-1.1 \pm 0.4$	$-1.0 \pm 0.1$
$\langle \beta_{spec} \rangle^a$	$-0.5 \pm 0.3$	$-0.6 \pm 0.3$	$-0.9 \pm 0.3$	$-0.3 \pm 0.3$	$-0.9 \pm 0.4$	$-0.4 \pm 0.2$
$\beta_{spec}^b$	$-0.1 \pm 0.4$	$-0.5 \pm 0.3$	$-0.7 \pm 0.3$	$-0.1 \pm 0.4$	$-0.7 \pm 0.5$	$-0.2 \pm 0.3$
$W_{Ly\alpha}^c$	$123 \pm 14$	$28 \pm 5$	$62 \pm 18$	$56 \pm 16$	$103 \pm 37$	$52 \pm 8$
$W_{NV,1240}^c$	$6.23 \pm 1.54$	$4.42 \pm 1.01$	$3.22 \pm 0.84$	$8.21 \pm 1.80$	$4.15 \pm 1.66$	$5.83 \pm 1.12$
$W_{NIV,1484}^c$	$2.13 \pm 0.86$	$1.68 \pm 0.53$	$1.05 \pm 0.52$	$2.51 \pm 1.17$	$3.07 \pm 1.36$	$1.57 \pm 0.58$
$W_{CIV,1549}^c$	$25.21 \pm 4.15$	$7.99 \pm 2.56$	$10.17 \pm 3.84$	$16.40 \pm 4.15$	$40.43 \pm 8.06$	$12.01 \pm 2.89$
$W_{HeII,1640}^c$	$9.16 \pm 1.88$	$5.48 \pm 1.71$	$6.01 \pm 1.23$	$8.13 \pm 3.09$	$14.03 \pm 5.29$	$6.27 \pm 1.41$
$W_{CIII,1909}^c$	$20.85 \pm 8.00$	$6.06 \pm 2.66$	$14.08 \pm 5.90$	$15.62 \pm 6.74$	$36.75 \pm 15.58$	$8.75 \pm 2.90$
$W_{SiII,1260}^c$	-	$-1.81 \pm 0.49$	$-0.87 \pm 0.34$	-	-	$-1.80 \pm 0.39$
$W_{OI+SiII,1303}^c$	$-2.00 \pm 0.82$	$-1.96 \pm 0.54$	$-2.36 \pm 0.47$	-	-	$-2.27 \pm 0.54$
$W_{SiIV,1393}^c$	-	$-1.72 \pm 0.74$	$-1.66 \pm 0.55$	-	-	$-1.34 \pm 0.67$
$W_{SiII,1527}^c$	-	$-1.03 \pm 0.53$	$-0.85 \pm 0.35$	-	-	$-0.79 \pm 0.35$

<sup>a</sup> Sample average values for the composite spectra.

<sup>b</sup> UV-continuum slope, measured from the composite spectra.

<sup>c</sup> Rest-frame EW in Å, measured from the composite spectra. Positive values indicate emission, while negative values indicate absorption. Uncertainties are calculated as described in §4.1. This table includes absorption and emission measurements with greater than  $2\sigma$  significance.

galaxies at  $z \sim 2 - 3$  (Shapley et al. 2003; Steidel et al. 2010). Thacker et al. (2006) presents results of a simulation that indicate that pure star formation, even when the full kinetic energy from each supernovae is applied to the outflowing material, can only produce maximum outflow velocities of roughly  $v = 600 \text{ km s}^{-1}$ . Their modeling shows that only AGNs and quasars can produce high speed outflows with velocities greater than  $10^3 \text{ km s}^{-1}$ . Outflows of this magnitude have also been seen in poststarburst galaxies at  $z = 0.6$ , using Mg II  $\lambda\lambda 2796, 2803$ , which are claimed to result from the effects of an AGN (Tremonti et al. 2007).

Previous studies of outflows observed in galaxies with AGNs can be used to place these UV-selected AGN results in context. Krug et al. (2010) presented a study of outflows from a sample of local IR-faint AGN. For the narrow-lined objects, the outflow velocities (as calculated from the Na I D interstellar absorption line doublet) are on the order of those from starburst galaxies, offering a conclusion that star formation was the process driving the outflows in Seyfert 2 systems. Based on a sample of local infrared-luminous starburst galaxies exhibiting AGN activity, Rupke et al. (2005a) show evidence for high velocity superwinds, which they compare to those from a non-AGN ULIRG sample presented in Rupke et al. (2005b,c). Both have comparable outflow velocities, leading to the conclusion that the momentum and energy required for the outflow could have come equally from a starburst or the AGN. The current work represents the same type of differential comparison between AGNs and their non-active counterparts, but at high redshift, when the black hole and bulge are both actively forming. This analysis highlights the specific effects of the AGN on the outflowing ISM. Relative to work on AGN outflows at high redshift, which has focused on the extended line emission in individual systems or small samples of AGNs alone (Alexander et al. 2010; Nesvadba et al. 2008), the benefit of our analysis

lies in our comparison to a control sample of non-AGN star-forming galaxies.

In order to understand how the outflows observed in our sample of AGNs will ultimately affect the galactic gas content, a calculation of the mass outflow rate of the gas is needed. Such a calculation requires knowledge of the outflowing gas metallicity, column density, covering fraction and physical location with respect to the illuminating source. Specifically, it is necessary to determine whether the outflowing gas extends over the scale of the entire galaxy or is confined to the scale of the central engine. Based on current data, we cannot obtain a precise estimate of the location of the gas, metallicity, column density, or covering fraction. Without determinations of these properties, a full comparison to AGN feedback models (e.g. Thacker et al. 2006) cannot be made.

The N IV]  $\lambda 1486$  emission line is detected in our AGN composite. This feature is not detected in the non-AGN LBG composite (Shapley et al. 2003), and is observed only rarely in broad-lined quasars in the Sloan Digital Sky Survey (Bentz et al. 2004; Jiang et al. 2008). At the same time, N IV] has been detected in the spectra of high redshift radio galaxies (Vernet et al. 2001; Humphrey et al. 2008). In order to determine the origin of the N IV] emission, Humphrey et al. (2008) consider both photoionization and shock models. A comparison of model predictions for line ratios such as N IV] / C IV and N IV] / He II with those measured in our composite spectrum suggests that the observed N IV] originates in photoionized gas. Our observed line ratios indicate that the gas is of solar or supersolar metallicity and subjected to a hard ionizing spectrum ( $f_\nu \propto \nu^\alpha$ , where  $\alpha \geq -1.0$ ) with ionization parameter  $U \geq 0.05$ , where  $U$  is defined here as the ratio of ionizing photons to H atoms at the surface of the model photoionized gas slab. On the other hand, shock excitation models cannot explain our high observed values of N IV] / C IV.

The EW of Ly $\alpha$  in the UV spectra of our AGNs is

indicative of both the strength of the AGN as well as the properties of star-forming regions. The observed Ly $\alpha$  EW is further modulated by various radiative transfer effects, due to its high scattering cross section. In non-AGN LBGs, the strength of Ly $\alpha$  emission has been shown to correlate with the EW of low-ionization interstellar absorption lines, such that strong Ly $\alpha$  emission is accompanied by weaker interstellar absorption (Shapley et al. 2003). This result can be understood if the escape of Ly $\alpha$  photons is at least partially modified by the covering fraction of neutral gas in the ISM. Additionally, Kornei et al. (2010) show that stronger Ly $\alpha$  emission is coupled with smaller dust obscuration as traced by the slope of the UV continuum, indicating that interaction with dust preferentially destroys Ly $\alpha$  photons, a result consistent with previous work by Shapley et al. (2003), Pentericci et al. (2007), and Verhamme et al. (2008).

When separating our objects according to Ly $\alpha$  EW to create composite spectra, we find that the composite spectrum created from objects with large Ly $\alpha$  EW shows stronger C III], C IV and He II emission than the composite spectrum created from objects with smaller Ly $\alpha$  EWs. As shown in Table 4, the C III], C IV, and He II lines are two to three times weaker in the  $W_{Ly\alpha} < 63$  composite spectrum than in the  $W_{Ly\alpha} > 63$  composite spectrum. This result suggests that the strength of Ly $\alpha$  emission is modulated at least partially by the level of AGN activity, which is traced by the strength of these other emission lines. However, the fact that the Ly $\alpha$  EW is almost 5 times weaker in the weak Ly $\alpha$  EW composite spectrum indicates additional suppression of Ly $\alpha$  photons beyond the reduced level of AGN activity. At the same time, the low-ionization interstellar absorption lines that indicate the covering fraction of cool gas are significantly stronger in the weak Ly $\alpha$  composite. Therefore, it is not only the strength of the underlying AGN that separates

the objects by Ly $\alpha$  EW, but also the covering fraction of gas that might absorb and reradiate the Ly $\alpha$  emission. This trend agrees with the results of Shapley et al. (2003) for non-AGN LBGs.

In our AGN sample, the UV continuum of the strong Ly $\alpha$  composite is redder than that of the weak Ly $\alpha$  composite, though the difference is not significant. This discrepancy with the trends among non-AGN LBGs from Shapley et al. (2003) and Kornei et al. (2010) may be a result of our small sample size, or potentially because the Ly $\alpha$  flux we observe originates from both the general star-forming ISM as well as the nuclear region. These two sources of Ly $\alpha$  photons may have disjoint properties with respect to the geometry of dust extinction, suppressing the trend observed among the non-AGN LBGs.

Future modeling of the spectral energy distributions of the AGN host galaxies (Hainline et al. in prep.) will allow for analysis of the UV spectra separated by stellar mass and E(B-V), as well as uncover spectral trends as a function of galaxy evolutionary state. We also will probe the origin of the strikingly red UV continuum slopes found in the narrow-line UV-selected AGN spectra.

We would like to thank Dawn Erb and Max Pettini for their helpful discussions. We would also like to acknowledge the referee, David Alexander, for a thorough and constructive report, which significantly improved the paper. A.E.S. acknowledges support from the David and Lucile Packard Foundation. C.C.S. acknowledges additional support from the John D. and Catherine T. MacArthur Foundation and the Peter and Patricia Gruber Foundation. We wish to extend special thanks to those of Hawaiian ancestry on whose sacred mountain we are privileged to be guests. Without their generous hospitality, most of the observations presented herein would not have been possible.

## REFERENCES

- Adelberger, K. L. & Steidel, C. C. 2005, *ApJ*, 627, L1  
 Adelberger, K. L., Steidel, C. C., Shapley, A. E., Hunt, M. P., Erb, D. K., Reddy, N. A., & Pettini, M. 2004, *ApJ*, 607, 226  
 Adelberger, K. L., Steidel, C. C., Shapley, A. E., & Pettini, M. 2003, *ApJ*, 584, 45  
 Aird, J., Nandra, K., Laird, E. S., Georgakakis, A., Ashby, M. L. N., Barmby, P., Coil, A. L., Huang, J., Koekemoer, A. M., Steidel, C. C., & Willmer, C. N. A. 2010, *MNRAS*, 401, 2531  
 Alexander, D. M., Swinbank, A. M., Smail, I., McDermid, R., & Nesvadba, N. P. H. 2010, *MNRAS*, 402, 2211  
 Allen, M. G., Dopita, M. A., & Tsvetanov, Z. I. 1998, *ApJ*, 493, 571  
 Assef, R. J., Kochanek, C. S., Brodwin, M., Cool, R., Forman, W., Gonzalez, A. H., Hickox, R. C., Jones, C., Le Floch, E., Moustakas, J., Murray, S. S., & Stern, D. 2009, *astro-ph:0909.3849*  
 Baldwin, J. A. 1977, *ApJ*, 214, 679  
 Bentz, M. C., Hall, P. B., & Osmer, P. S. 2004, *AJ*, 128, 561  
 Buson, L. M. & Ulrich, M. 1990, *A&A*, 240, 247  
 Calzetti, D., Kinney, A. L., & Storchi-Bergmann, T. 1994, *ApJ*, 429, 582  
 Chandar, R., Leitherer, C., Tremonti, C. A., Calzetti, D., Aloisi, A., Meurer, G. R., & de Mello, D. 2005, *ApJ*, 628, 210  
 Crenshaw, D. M., Kraemer, S. B., & George, I. M. 2003, *ARA&A*, 41, 117  
 Croton, D. J., Springel, V., White, S. D. M., De Lucia, G., Frenk, C. S., Gao, L., Jenkins, A., Kauffmann, G., Navarro, J. F., & Yoshida, N. 2006, *MNRAS*, 365, 11  
 Davidson, K., Dufour, R. J., Walborn, N. R., & Gull, T. R. 1986, *ApJ*, 305, 867  
 Di Matteo, T., Colberg, J., Springel, V., Hernquist, L., & Sijacki, D. 2008, *ApJ*, 676, 33  
 Fosbury, R. A. E., Villar-Martín, M., Humphrey, A., Lombardi, M., Rosati, P., Stern, D., Hook, R. N., Holden, B. P., Stanford, S. A., Squires, G. K., Rauch, M., & Sargent, W. L. W. 2003, *ApJ*, 596, 797  
 Franx, M., Illingworth, G. D., Kelson, D. D., van Dokkum, P. G., & Tran, K. 1997, *ApJ*, 486, L75  
 Ganguly, R. & Brotherton, M. S. 2008, *ApJ*, 672, 102  
 Glikman, E., Djorgovski, S. G., Stern, D., Bogosavljević, M., & Mahabal, A. 2007, *ApJ*, 663, L73  
 Groves, B. A., Dopita, M. A., & Sutherland, R. S. 2004, *ApJS*, 153, 75  
 Gültekin, K., Richstone, D. O., Gebhardt, K., Lauer, T. R., Tremaine, S., Aller, M. C., Bender, R., Dressler, A., Faber, S. M., Filippenko, A. V., Green, R., Ho, L. C., Kormendy, J., Magorrian, J., Pinkney, J., & Siopis, C. 2009, *ApJ*, 698, 198  
 Hamann, F., Korista, K. T., Ferland, G. J., Warner, C., & Baldwin, J. 2002, *ApJ*, 564, 592  
 Hopkins, P. F., Hernquist, L., Cox, T. J., & Kereš, D. 2008, *ApJS*, 175, 356  
 Humphrey, A., Villar-Martín, M., Vernet, J., Fosbury, R., di Serego Alighieri, S., & Binette, L. 2008, *MNRAS*, 383, 11  
 Jiang, L., Fan, X., & Vestergaard, M. 2008, *ApJ*, 679, 962  
 Kauffmann, G., Heckman, T. M., Tremonti, C., Brinchmann, J., Charlot, S., White, S. D. M., Ridgway, S. E., Brinkmann, J., Fukugita, M., Hall, P. B., Ivezić, Z., Richards, G. T., & Schneider, D. P. 2003, *MNRAS*, 346, 1055  
 Korista, K. T., Bautista, M. A., Arav, N., Moe, M., Costantini, E., & Benn, C. 2008, *ApJ*, 688, 108

- Kormendy, J. & Richstone, D. 1995, *ARA&A*, 33, 581
- Kornei, K. A., Shapley, A. E., Erb, D. K., Steidel, C. C., Reddy, N. A., Pettini, M., & Bogosavljević, M. 2010, *ApJ*, 711, 693
- Krug, H. B., Rupke, D. S. N., & Veilleux, S. 2010, *ApJ*, 708, 1145
- Madau, P., Ferguson, H. C., Dickinson, M. E., Giavalisco, M., Steidel, C. C., & Fruchter, A. 1996, *MNRAS*, 283, 1388
- Martin, C. L. 2005, *ApJ*, 621, 227
- Matsuoka, K., Nagao, T., Maiolino, R., Marconi, A., & Taniguchi, Y. 2009, *A&A*, 503, 721
- McLean, I. S., Becklin, E. E., Bendiksen, O., Brims, G., Canfield, J., Figer, D. F., Graham, J. R., Hare, J., Lacayanga, F., Larkin, J. E., Larson, S. B., Levenson, N., Magnone, N., Teplitz, H., & Wong, W. 1998, in *Proc. SPIE Vol. 3354*, p. 566-578, *Infrared Astronomical Instrumentation*, Albert M. Fowler; Ed., Vol. 3354, 566-578
- Merritt, D. & Ferrarese, L. 2001, *ApJ*, 547, 140
- Murray, N., Quataert, E., & Thompson, T. A. 2005, *ApJ*, 618, 569
- Nagao, T., Maiolino, R., & Marconi, A. 2006a, *A&A*, 447, 863
- Nagao, T., Marconi, A., & Maiolino, R. 2006b, *A&A*, 447, 157
- Nesvadba, N. P. H., Lehnert, M. D., De Breuck, C., Gilbert, A. M., & van Breugel, W. 2008, *A&A*, 491, 407
- Nesvadba, N. P. H., Lehnert, M. D., Eisenhauer, F., Gilbert, A., Tecza, M., & Abuter, R. 2006, *ApJ*, 650, 693
- Nilsson, K. K., Tapken, C., Møller, P., Freudling, W., Fynbo, J. P. U., Meisenheimer, K., Laursen, P., & Östlin, G. 2009, *A&A*, 498, 13
- Oke, J. B., Cohen, J. G., Carr, M., Cromer, J., Dingizian, A., Harris, F. H., Labrecque, S., Lucinio, R., Schaal, W., Epps, H., & Miller, J. 1995, *PASP*, 107, 375
- Pentericci, L., Grazian, A., Fontana, A., Salimbeni, S., Santini, P., de Santis, C., Gallozzi, S., & Giallongo, E. 2007, *A&A*, 471, 433
- Pettini, M., Rix, S. A., Steidel, C. C., Adelberger, K. L., Hunt, M. P., & Shapley, A. E. 2002, *ApJ*, 569, 742
- Pettini, M., Shapley, A. E., Steidel, C. C. and Čuby, J.-G., Dickinson, M., Moorwood, A. F. M. and Adelberger, K. L., & Giavalisco, M. 2001, *ApJ*, 554, 981
- Pettini, M., Steidel, C. C., Adelberger, K. L., Dickinson, M., & Giavalisco, M. 2000, *ApJ*, 528, 96
- Raiter, A., Fosbury, R. A. E., & Teimoorinia, H. 2010, *A&A*, 510, A109+
- Reddy, N. A., Steidel, C. C., Pettini, M., Adelberger, K. L., Shapley, A. E., Erb, D. K., & Dickinson, M. 2008, *ApJS*, 175, 48
- Richards, G. T., Lacy, M., Storrie-Lombardi, L. J., Hall, P. B., Gallagher, S. C., Hines, D. C., Fan, X., Papovich, C., Vanden Berk, D. E., Trammell, G. B., Schneider, D. P., Vestergaard, M., York, D. G., Jester, S., Anderson, S. F., Budavári, T., & Szalay, A. S. 2006, *ApJS*, 166, 470
- Rupke, D. S., Veilleux, S., & Sanders, D. B. 2005a, *ApJ*, 632, 751
- . 2005b, *ApJS*, 160, 87
- . 2005c, *ApJS*, 160, 115
- Shapley, A. E., Steidel, C. C., Pettini, M., & Adelberger, K. L. 2003, *ApJ*, 588, 65
- Silk, J. & Rees, M. J. 1998, *A&A*, 331, L1
- Silverman, J. D., Green, P. J., Barkhouse, W. A., Kim, D., Kim, M., Wilkes, B. J., Cameron, R. A., Hasinger, G., Jannuzi, B. T., Smith, M. G., Smith, P. S., & Tananbaum, H. 2008, *ApJ*, 679, 118
- Somerville, R. S., Hopkins, P. F., Cox, T. J., Robertson, B. E., & Hernquist, L. 2008, *MNRAS*, 391, 481
- Steidel, C. C., Adelberger, K. L., Shapley, A. E., Pettini, M., Dickinson, M., & Giavalisco, M. 2003, *ApJ*, 592, 728
- Steidel, C. C., Erb, D. K., Shapley, A. E., Pettini, M., Reddy, N., Bogosavljević, M., Rudie, G. C., & Racic, O. 2010, *ApJ*, 717, 289
- Steidel, C. C., Hunt, M. P., Shapley, A. E., Adelberger, K. L., Pettini, M., Dickinson, M., & Giavalisco, M. 2002, *ApJ*, 576, 653
- Steidel, C. C., Shapley, A. E., Pettini, M., Adelberger, K. L., Erb, D. K., Reddy, N. A., & Hunt, M. P. 2004, *ApJ*, 604, 534
- Thacker, R. J., Scannapieco, E., & Couchman, H. M. P. 2006, *ApJ*, 653, 86
- Tremonti, C. A., Moustakas, J., & Diamond-Stanic, A. M. 2007, *ApJ*, 663, L77
- Ueda, Y., Akiyama, M., Ohta, K., & Miyaji, T. 2003, *ApJ*, 598, 886
- Vanzella, E., Giavalisco, M., Dickinson, M., Cristiani, S., Nonino, M., Kuntschner, H., Popesso, P., Rosati, P., Renzini, A., Stern, D., Cesarsky, C., Ferguson, H. C., & Fosbury, R. A. E. 2009, *ApJ*, 695, 1163
- Verhamme, A., Schaerer, D., Atek, H., & Tapken, C. 2008, *A&A*, 491, 89
- Vernet, J., Fosbury, R. A. E., Villar-Martín, M., Cohen, M. H., Cimatti, A., di Serego Alighieri, S., & Goodrich, R. W. 2001, *A&A*, 366, 7
- Villar-Martín, M., Alonso-Herrero, A., di Serego Alighieri, S., & Vernet, J. 2000, *A&AS*, 147, 291
- Villar-Martín, M., Tadhunter, C., & Clark, N. 1997, *A&A*, 323, 21
- Villar-Martín, M., Vernet, J., di Serego Alighieri, S., Fosbury, R., Humphrey, A., & Pentericci, L. 2003, *MNRAS*, 346, 273